A Photometric Study of the Eclipsing Binary QT Ursae Majoris

Edward J. Michaels
Stephen F. Austin State University, Department of Physics, Engineering and Astronomy, P.O. Box 13044, Nacogdoches, TX 75962; emichaels@sfasu.edu

Received June 6, 2017; revised July 25, 2017; accepted July 25, 2017

Abstract Presented are the first multiband light curves of the eclipsing binary QT Ursae Majoris. The light curves were analyzed using the Wilson-Devinney program to find the best-fit stellar model. Asymmetries in the light curves required spots to be included in the model. The solution results give a Roche Lobe fill-out of 13%, which is consistent with a W-type contact binary. New linear and quadratic ephemerides were computed using 31 times of minima, including 8 new ones from this study.

1. Introduction

The variability of QT UMa (GSC 03429-0424) was discovered in the Northern Sky Variability Survey database (NSVS; Wozniak *et al.* 2004) (Otero *et al.* 2004). This star was classified as an EW eclipsing binary with a magnitude range of 11.0–11.8. An automated variable star classification method also found the star to be a W UMa type binary (Hoffman *et al.* 2009). The orbital period, 0.473522 d, was determined from the NSVS data (Otero *et al.* 2004). The light curve was reported to show a slight O'Connell effect. From Tycho 2 data this star's effective temperature was found to be 6065 K with a color excess of E(B–V) = 0.006 (Ammons *et al.* 2006). The LAMOST spectroscopic survey gives an effective temperature of 5493 K (Luo *et al.* 2015) (Sichervskij 2017). A parallax measurement from the first data release of the Gaia mission gives a distance of 247 ± 15 pc (Gaia Data Release 1; Gaia Collaboration *et al.*, 2016) (Astraatmadja and Bailer-Jones 2016).

In this paper, a photometric study of QT UMa is presented in organized sections. Section 2 presents the first set of multi-wavelength photometric observations for this star, new ephemerides are presented in section 3, a light curve analysis is given in section 4, and conclusions in section 5.

Table 1. Stars used in this study.

Star	*R.A. (2000) h m s*	*Dec. (2000) ° ′ ″*	*g′*	*r′*	*i′*
QT UMa	09 36 29.2	+48 52 46			
[1]GSC 3429-1671 (C1)	09 35 49.4	+48 55 33	11.405 ± 0.063	10.773 ± 0.055	10.535 ± 0.038
[1]GSC 3429-0263 (C2)	09 37 15.4	+48 48 43	11.428 ± 0.090	11.057 ± 0.053	10.973 ± 0.040
[1]GSC 3429-1192 (C3)	09 36 51.3	+48 43 42	12.447 ± 0.060	11.677 ± 0.044	11.418 ± 0.030
[1]GSC 3429-1426 (C4)	09 35 48.2	+48 48 25	12.476 ± 0.052	11.945 ± 0.055	11.788 ± 0.040
[2]GSC 3429-0822 (K)	09 36 54.8	+48 45 05	12.530 ± 0.062	11.830 ± 0.048	11.592 ± 0.036
Observed check star (K) magnitudes			12.533 ± 0.036	11.832 ± 0.027	11.596 ± 0.022
Standard deviation of check star magnitudes			± 0.008	± 0.009	± 0.009

APASS [1]comparison stars (C1–C4) and [2]check star (K) magnitudes and errors.

2. Observations

Photometric observations were acquired using the 0.31-m Ritchey-Chrétien robotic telescope at the Waffelow Creek Observatory (http://obs.ejmj.net/index.php). A SBIG-STXL camera equipped with a cooled KAF-6303E CCD (–30° C) was used for imaging on five nights in 2016, February 25, 26, 27, and March 1 and 3. A total of 2,957 images were obtained in three passbands: 966 in Sloan g', 995 in Sloan r', and 966 in Sloan i'. This data set was used in the light curve analysis in section 4 of this paper. Additional images were acquired in February 2015 and February 2017. These observations provided additional times of minima. Bias, dark, and flat frames were obtained before each night's observing run. Calibration and ensemble differential aperture photometry of the light images was performed using MIRA software (Mirametrics 2015). Table 1 contains the comparison and check stars used in this study, with a finder chart shown in Figure 1. The standard magnitudes of these stars were taken from the AAVSO Photometric All-

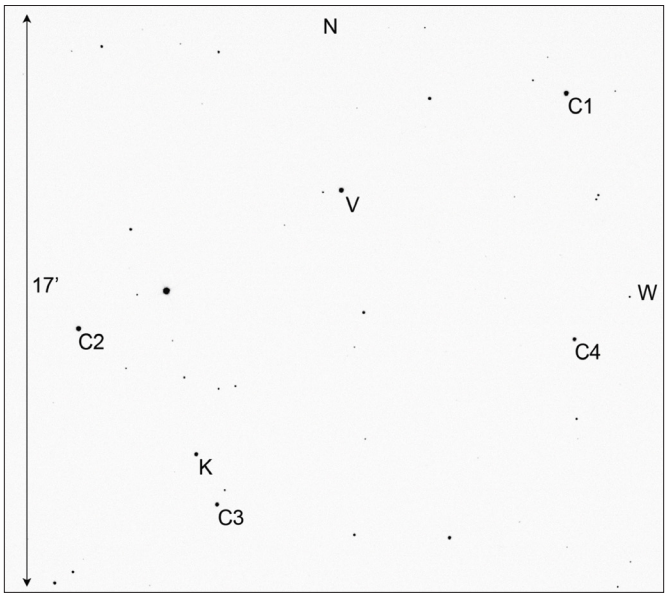

Figure 1. Finder chart for QT UMa (V), comparison (C1–C4), and check (K) stars.

Sky Survey (APASS) database (Henden *et al.* 2015). The instrumental magnitudes of QT UMa were converted to standard magnitudes using these comparison stars. The Heliocentric Julian Date (T) of each observation was converted to orbital phase using an epoch of T_o = 2457446.7202 and an orbital period of P = 0.4735397 d. Figure 2 shows the folded light curves in standard magnitudes. All light curves in this paper are plotted from phase –0.6 to 0.6 with negative orbital phase defined as φ – 1. The bottom panel of Figure 2 shows the Sloan r' check star magnitudes for all nights. Plots of the check star magnitudes were inspected each night but no significant variability was found. The 2016 observations in this study can be accessed from the AAVSO International Database (Kafka 2016).

3. Ephemerides

The Heliocentric Julian Date (HJD) of eight new times of minimum light were determined from the observations. These values are listed in Table 2 along with all minima times available in the literature. Figure 3 shows the O–C residuals calculated from the linear ephemeris of Otero et. al (2004) given by

$$\text{HJD Min I} = 2451563.948 + 0.473522E \; . \qquad (1)$$

From the residuals of Equation 1 a new linear ephemeris was computed by least-squares solution and is given by

$$\text{HJD Min I} = 2457446.7202(5) + 0.4735397(2)E \; . \qquad (2)$$

The best-fit linear line from Equation 2 is the dotted line in Figure 3. Using the residuals from Equation 2, a second least-squares solution gives the following quadratic ephemeris:

$$\text{HJD Min I} = 2457446.7169(5) + 0.4735417(5)E + 3.0(6) \times 10^{-9} E^2. \qquad (3)$$

Figure 4 shows the general trend of the O–C residuals from the new quadratic ephemeris which has a positive curve.

4. Analysis

4.1. Temperature, spectral type

The effective temperature of the larger secondary star was determined from the observed (g'–r') color at primary eclipse. The primary eclipse is nearly total, therefore most of the system light at orbital phase φ = 0 is from the secondary star. To determine the secondary star's color, the phase and magnitude of the g' and r' observations were binned with a phase width of 0.01. The phases and magnitudes in each bin interval were averaged. Figure 5 shows the resulting binned r' magnitude light curve with the bottom panel showing the (g'–r') color index. The observed color at primary eclipse is (g'–r') = 0.592 ± 0.012. The equation,

$$(B–V) = \frac{(g'–r') + 0.23}{1.09}, \qquad (4)$$

was used to transform the observed (g'–r') color to (B–V) = 0.754 ± 0.015 (Jester *et al.* 2005). The color excess, E(B–V)

Table 2. Times of minima and O–C residuals from Equation 2.

Epoch HJD 2400000+	*Error*	*Cycle*	*O–C Linear*	*References*
55932.8144	0.00020	0.0	0.00054	Nelson 2013
55944.8923	0.00040	25.5	0.00318	Diethelm 2012
56002.6601	0.00100	147.5	–0.00087	Hübscher 2013
56029.6547	0.00020	204.5	0.00197	Diethelm 2012
56311.8814	0.00020	800.5	–0.00098	Diethelm 2013
56706.5770	0.00460	1634.0	–0.00070	Hübscher and Lehmann 2015
56709.4202	0.00040	1640.0	0.00126	Hübscher and Lehmann 2015
56711.3104	0.00110	1644.0	–0.00270	Hübscher and Lehmann 2015
56728.5957	0.00010	1680.5	–0.00160	Hübscher 2016
57029.7681	0.00020	2316.5	–0.00043	Samolyk 2016b
57030.0043	0.00120	2317.0	–0.00100	Samolyk 2016b
57035.4491	0.00070	2328.5	–0.00191	Hübscher 2016
57035.6872	0.00020	2329.0	–0.00058	Hübscher 2016
57067.8880	0.00004	2397.0	–0.00050	Present paper
57072.8604	0.00004	2407.5	–0.00024	Present paper
57090.3807	0.00070	2444.5	–0.00091	Hübscher 2016
57121.3985	0.00100	2510.0	0.00004	Hübscher 2017
57132.5256	0.00010	2533.5	–0.00104	Hübscher 2017
57386.1063	—	3069.0	–0.00084	Nagai 2016
57386.3447	—	3069.5	0.00079	Nagai 2016
57415.7038	0.00010	3131.5	0.00043	Samolyk 2016a
57423.2811	—	3147.5	0.00109	Juryšek 2017
57444.8263	0.00010	3193.0	0.00027	Present paper
57445.7734	0.00009	3195.0	0.00024	Present paper
57446.7205	0.00012	3197.0	0.00026	Present paper
57465.4249	0.00250	3236.5	–0.00014	Hübscher 2017
57449.7989	0.00012	3203.5	0.00066	Present paper
57451.6929	0.00012	3207.5	0.00053	Present paper
57474.4227	—	3255.5	0.00041	Juryšek 2017
57498.5735	0.00400	3306.5	0.00069	Samolyk 2016b
57807.7963	0.00004	3959.5	0.00208	Present paper

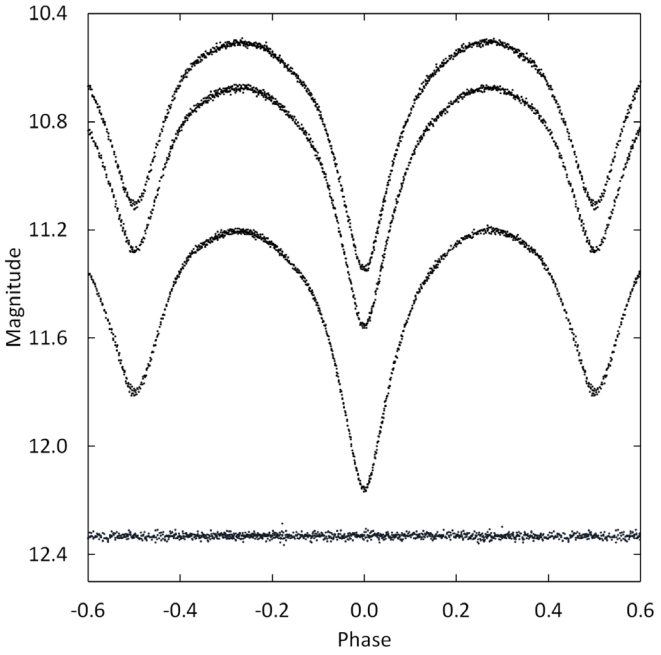

Figure 2. Folded light curves for each observed passband. The differential magnitudes of the variable were converted to standard magnitudes using the calibrated magnitudes of the comparison stars. From top to bottom the light curve passbands are Sloan i', Sloan r', Sloan g'. The bottom curve shows the Sloan r' magnitudes of the check star (offset +0.7 magnitudes). The standard deviations of the check star magnitudes (all nights) are shown in Table 1. Error bars are not shown for clarity.

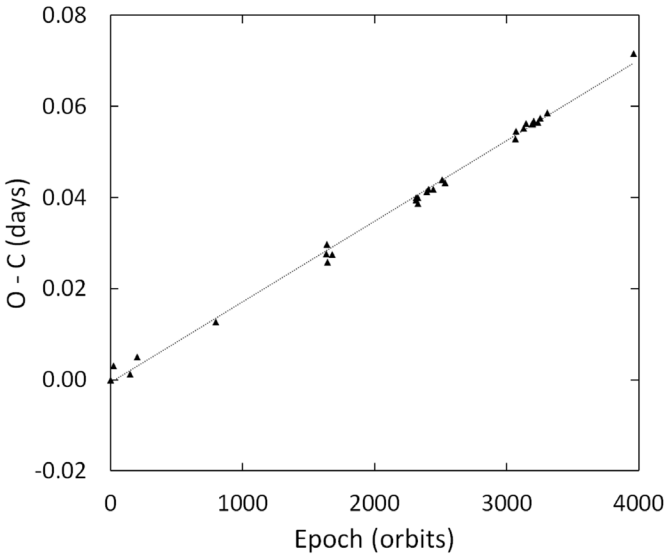

Figure 3. The O–C residuals from Equation 1 with the dotted line the linear ephemeris fit of Equation 2.

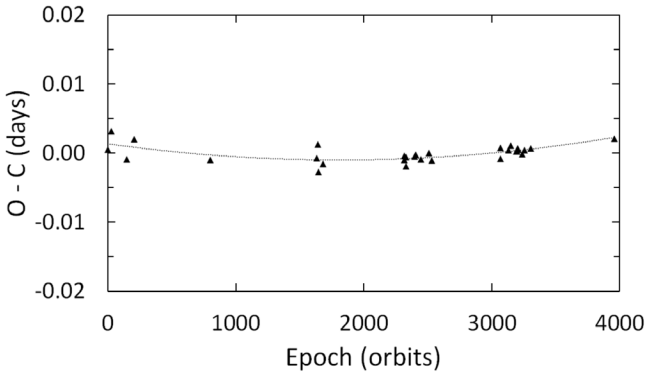

Figure 4. The O–C residuals from Equation 2 with the dotted line the quadratic ephemeris fit of Equation 3.

= 0.021 ± 0.052, was determined from Schlafly's (2014) map of interstellar reddening. This gives the secondary star's color as (B–V) = 0.733 ± 0.054 and an effective temperature of T_{eff} = 5497 ± 171K (Pecaut and Mamajek 2013). This value agrees well with the effective temperature determined from LAMOST spectral survey data, T_{eff} = 5493 ± 241K (Sichervskij 2017). Assuming the secondary is a main-sequence star, the corrected color index gives a spectral type of G8 (Table 5 of Pecaut and Mamajek 2013).

4.2. Synthetic light curve modeling

For light curve modeling, the Sloan g', r', and i' observations acquired in 2016 were binned in both phase and magnitude. A bin phase width of 0.005 was used which resulted in five observations per bin on average. The binned magnitudes were converted to relative flux for modeling. A preliminary fit to each individual light curve was made using BINARY MAKER 3.0 (BM3; Bradstreet and Steelman 2002). Standard convective parameters and tabulated limb darkening coefficients determined by the effective temperatures were utilized in the models. Once a reasonable fit was made for each light curve, the resulting stellar parameters were averaged. These parameters were used as the

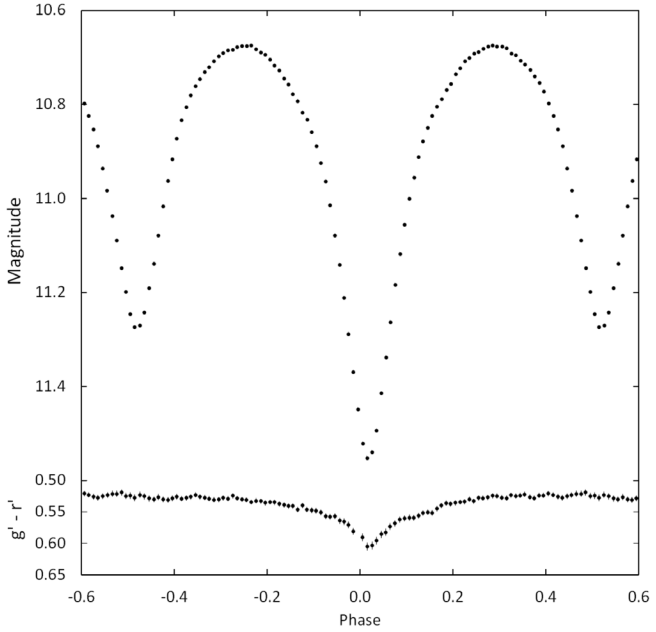

Figure 5. Light curve of all r'-band observations in standard magnitudes (top panel). The observations were binned with a phase width of 0.01. The errors for each binned point are about the size of the plotted points. The g'–r' colors were calculated by subtracting the binned Sloan g' magnitudes from the linearly interpolated binned Sloan r' magnitudes.

initial values for computation of a simultaneous three-color light curve solution using the Wilson-Devinney program (WD; Wilson and Devinney 1971; van Hamme and Wilson 1998). Mode 3, the contact configuration, was set in this program. A common convective envelope was assumed. The weight assigned to each input data point was equal to the number of observations that formed that point. The Method of Multiple Subsets (MMS) was utilized to minimize strong correlations, and the Kurucz stellar atmosphere model was applied (Wilson and Biermann 1976). For fixed inputs, the effective temperature of the secondary star was set to T_2 = 5497 K (see section 4.1) and standard convective values for gravity darkening and albedo, $g_1 = g_2 = 0.32$ (Lucy 1968) and $A_1 = A_2 = 0.5$ (Ruciński 1969), respectively. Logarithmic limb darkening coefficients were calculated by the program from tabulated values using the method of van Hamme (1993). The adjustable parameters include the inclination (i), mass ratio ($q = M_2/M_1$), potential (Ω), temperature of the primary star (T_1), the normalized flux for each wavelength (L), and third light (ℓ). To determine the system's approximate mass ratio (q), a series of WD solutions were made using fixed values that ranged from 0.4 to 2.8 with a step size of 0.10. Figure 6 shows the result of this q-search, which gave a minimum residual value for a mass ratio of 1.7. This value was used as the starting point for the final solution iterations where the mass ratio was a free parameter. The final WD solution parameters are listed in column 2 of Table 3. No third light was seen in the solution. Only negligible or negative values resulted when included as an adjustable parameter. The filling-factor in Table 3 was computed using

$$f = \frac{\Omega_{inner} - \Omega}{\Omega_{inner} - \Omega_{outer}}, \quad (5)$$

where Ω_{inner} and Ω_{outer} are the inner and outer critical equipotential

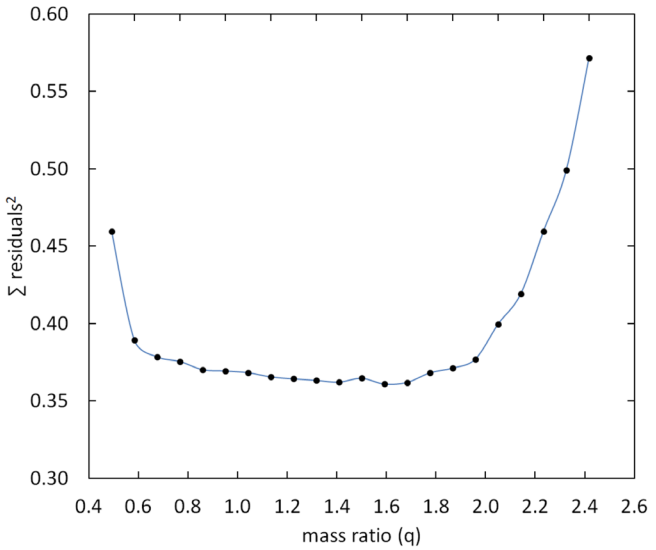

Figure 6. Results of the q-search showing the relation between the sum of the residuals squared and the mass ratio q.

Table 3. Results derived from light curve modeling.

Parameter	*Solution 1 (no spots)*	*Solution 2 (2 spots)*
phase shift	0.0005 ± 0.0002	0.0005 ± 0.0001
i (°)	82.0 ±0.2	81.9 ±0.2
T_1 (K)	6117 ±12	6053 ±20
T_2 (K)	* 5497	* 5497
$\Omega_1 = \Omega_2$	4.76 ± 0.05	4.75 ± 0.01
q(M2/M1)	1.72 ± 0.04	1.71 ± 0.01
filling factor	13%	13%
$L_1 / (L_1 + L_2)$ (g')	0.526 ±0.002	0.523 ±0.003
$L_1 / (L_1 + L_2)$ (r')	0.488 ±0.002	0.485 ±0.002
$L_1 / (L_1 + L_2)$ (i')	0.471 ±0.002	0.470 ±0.002
r_1 side	0.3225 ±0.0012	0.3309 ±0.0006
r_2 side	0.5233 ±0.0104	0.4391 ±0.0024
$\sum res^2$	0.318	0.060
Spot Parameters	—	*Star 1—cool spot*
colatitude (°)	—	112 ± 17
longitude (°)	—	359 ± 1
spot radius (°)	—	34 ± 7
Temp.-factor	—	0.95 ± 0.04
Spot Parameters		*Star 2—hot spot*
colatitude (°)	—	78 ± 6
longitude (°)	—	0.2 ± 0.2
spot radius (°)	—	34 ± 5
Temp.-factor	—	1.10 ± 0.02

** Assumed.*

The subscripts 1 and 2 refer to the star being eclipsed at primary and secondary minimum, respectively.

Note: The errors in the stellar parameters result from the least squares fit to the model. The actual uncertainties of the parameters are considerably larger (T1 and T2 have uncertainties of about ± 170 K).

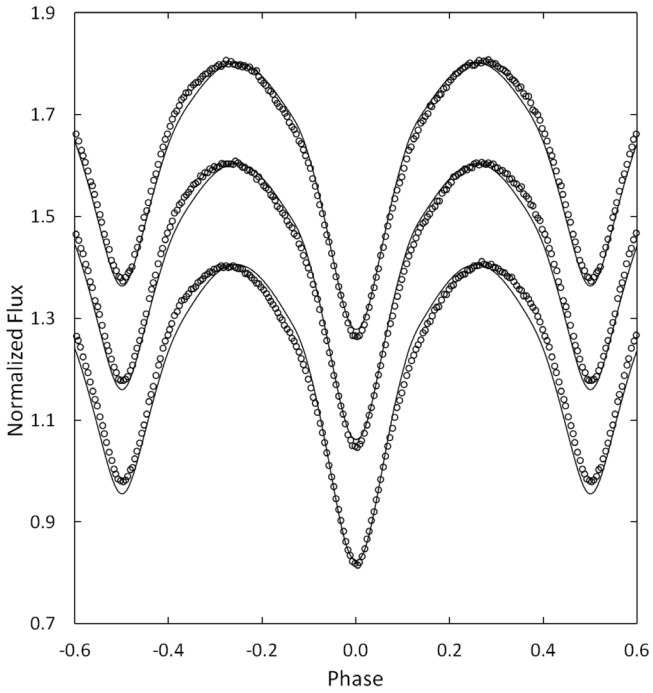

Figure 7. The WD model fit without spots (solid curve) to the observed normalized flux curves for each passband. From top to bottom the passbands are Sloan i', Sloan r', and Sloan g'. Each curve is offset by 0.2 for this combined plot. The best-fit parameters are given in column 2 of Table 3. Error bars are omitted from the points for clarity.

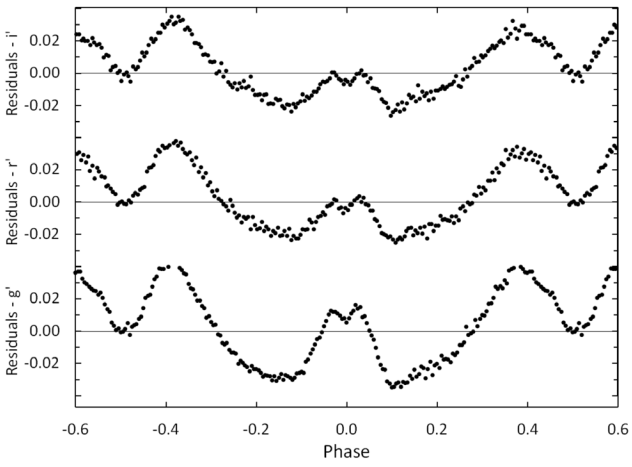

Figure 8. The residuals for the best-fit WD model without spots. Error bars are omitted from the points for clarity.

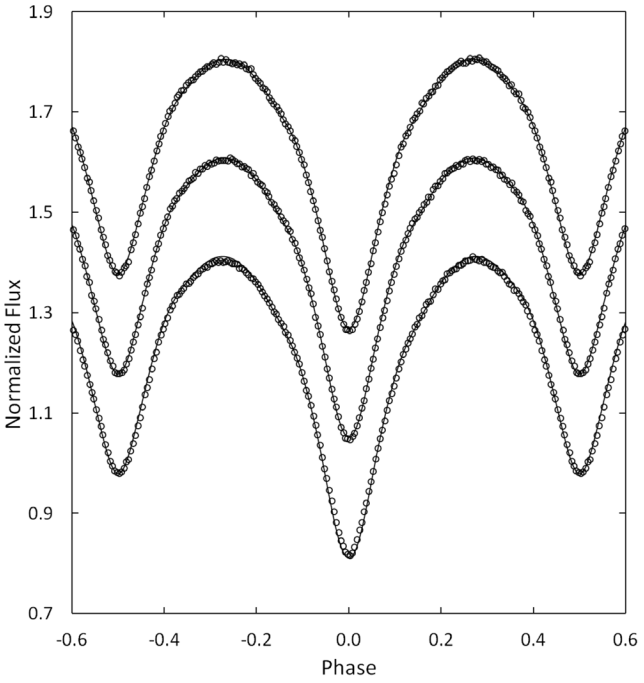

Figure 9. The WD model fit with spots (solid curve) to the observed normalized flux curves for each passband. From top to bottom the passbands are Sloan i', Sloan r', and Sloan g'. Each curve is offset by 0.2 for this combined plot. The best-fit parameters are given in column 3 of Table 3. Error bars are omitted from the points for clarity.

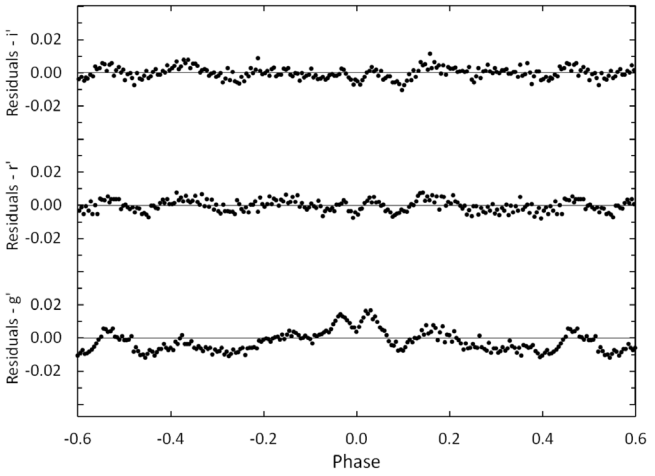

Figure 10. The residuals for the spotted WD model in each passband. Error bars are omitted from the points for clarity.

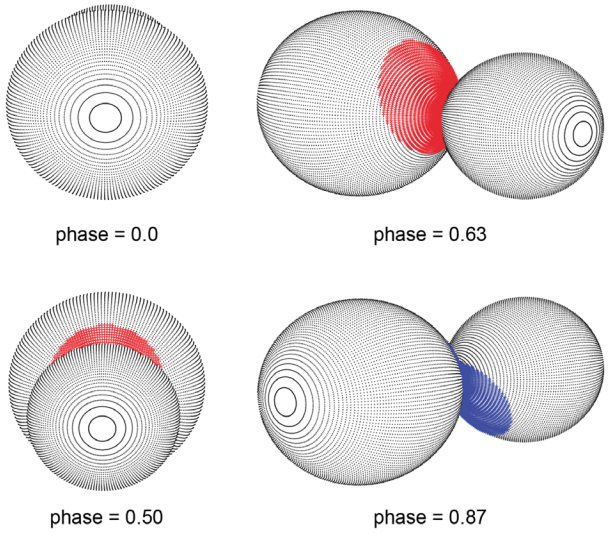

Figure 11. Roche Lobe surfaces of the best-fit WD spot model with orbital phase shown below each diagram.

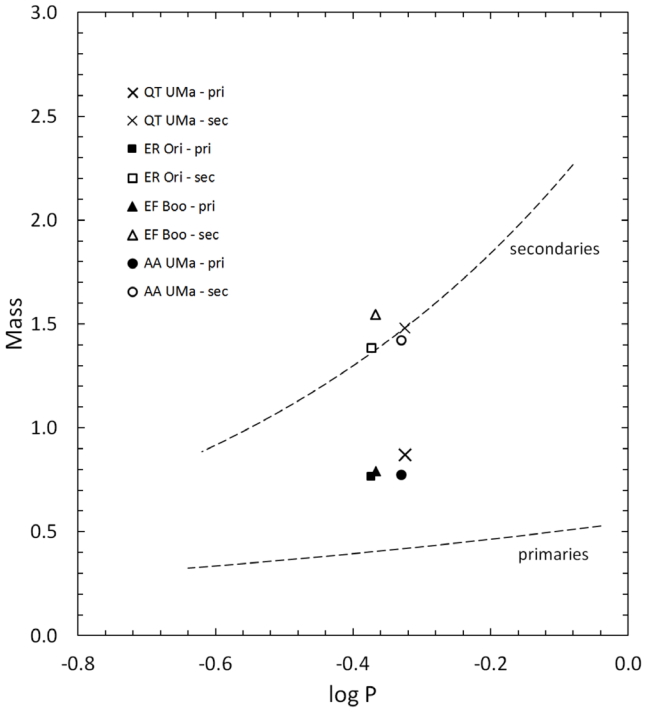

Figure 12. Comparison of the primary and secondary masses of four contact binaries. The dashed lines are the primary and secondary star period-mass relations for contact binaries (Gazeas and Stępień 2008). The masses are in solar units.

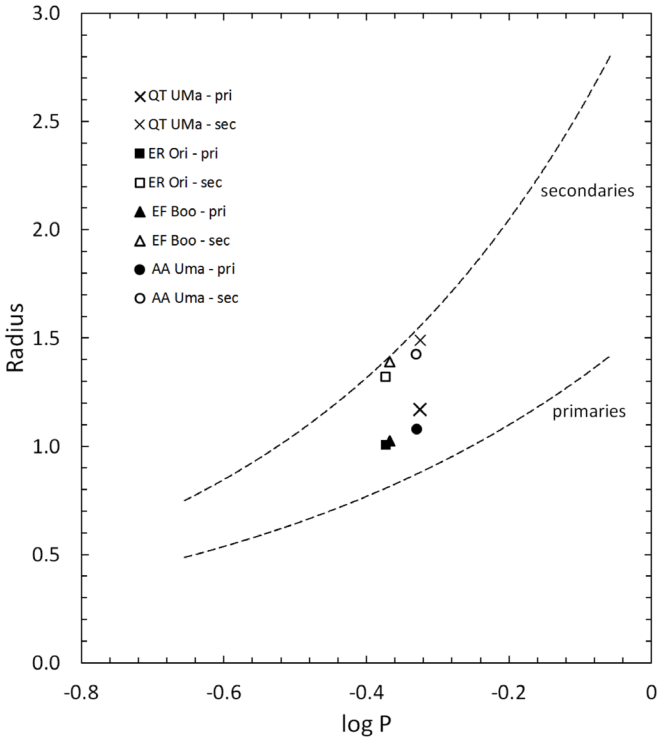

Figure 13. Comparison of the primary and secondary radii of four contact binaries. The dashed lines are the primary and secondary star period-radius relations for contact binaries (Gazeas and Stępień 2008). The radii are in solar units.

surfaces that pass through the Lagrangian points L_1 and L_2 and Ω is the equipotential surface which describes the stellar surface (Lucy and Wilson 1979). The normalized light curves for each passband, overlaid by the synthetic solution curves, are shown in Figure 7 with the residuals shown in Figure 8.

4.3. Spot model

Considerable asymmetries are apparent in the light curves. These are usually attributed to cool spots or hot spots such as faculae on the stars. Best seen in the residuals of Figure 8, there are two broad regions where the observations deviate from the synthetic light curves. First, there is excess light centered on secondary eclipse (φ = 0.5) with a phase width of approximately 0.2. This indicates a possible over luminous region on the cooler secondary star located near the line of centers between the two stars. The second region is under luminous and is centered on primary eclipse with a phase width of 0.8. This would indicate a possible cool spot located on the hotter primary star, also near the line of centers. Using BM3, two spots were modeled in these two locations. The resulting best-fit spot parameters of latitude, longitude, size, and temperature-factor were then incorporated into a new WD model. Initially the stellar parameters in the WD solution iterations were held fixed, with only the lights and spot parameters adjusted. Once this solution converged, the spot parameters were then held fixed and the stellar parameters adjusted until the solution converged again. This process was repeated until the model converged to a final solution. The new spotted solution parameters are listed in column 3 of Table 3. The normalized light curves overlaid by the synthetic solution curves are shown in Figure 9 and the residuals in Figure 10. The residuals are 5.3 times smaller compared to the spotless solution

Table 4. Estimated absolute parameters for QT UMa.

Parameter	*Symbol*	*Value*
Stellar masses	M_1 ($M_\odot$)	0.87 ± 0.07
	M_2 ($M_\odot$)	1.48 ± 0.11
Semi-major axis	a ($R_\odot$)	3.40 ± 0.01
Mean stellar radii	R_1 ($R_\odot$)	1.17 ± 0.01
	R_2 ($R_\odot$)	1.49 ± 0.02
Stellar luminosity	L_1 ($L_\odot$)	1.66 ± 0.11
	L_2 ($L_\odot$)	1.82 ± 0.17
Bolometric magnitude	$M_{bol,1}$	4.21 ± 0.12
	$M_{bol,2}$	4.10 ± 0.19
Surface gravity	log g_1 (cgs)	4.24 ± 0.03
	log g_2 (cgs)	4.26 ± 0.04
Mean density	$\bar{\rho}_1$ (g cm^{-3})	0.76 ± 0.04
	$\bar{\rho}_2$ (g cm^{-3})	0.63 ± 0.07

The calculated values in this table are provisional. Radial velocity observations are necessary for direct determination of M_1, M_2, and a.

with a much improved fit between the synthetic and observed light curves. The Roche lobe surfaces from this solution are displayed in Figure 11.

5. Discussion and conclusions

Radial velocity measurements are not available for this star, but the absolute mass of the more massive secondary star (M2) can be estimated from the orbital period. The period-mass relation for contact binaries,

$$M_2 = (0.755 \pm 0.059) \log P + (0.416 \pm 0.024), \qquad (6)$$

gives a provisional mass for the secondary star of $M_2 = 1.48 \pm 0.11 M_\odot$ (Gazeas and Stępień 2008). The remaining absolute parameter values can now be determined. Combining the secondary star's mass with the mass ratio from the spotted solution gives the primary star's mass as $M_1 = 0.87 \pm 0.07 M_\odot$. Kepler's Third Law gives a distance of $3.398 \pm 0.007 R_\odot$ between the mass centers of the two stars. The WD light curve program (LC) computed the stellar radii, surface gravities, and bolometric magnitudes. The mean stellar densities were determined from the following equations,

$$\bar{\rho}_1 = \frac{0.0189}{r_1^3 (1 + q) P^2} \quad \text{and} \quad \bar{\rho}_2 = \frac{0.0189q}{r_2^3 (1 + q) P^2}, \qquad (7)$$

where the stellar radius is normalized to the semi-major axis and P is in days (Mochnacki 1981). Table 4 contains all the calculated stellar parameter values. To assess the reasonableness of the masses, radii and the mass ratio found in this study, it is useful to compare QT UMa to a number of similar contact binaries. Figure 12 shows the period-mass relation and Figure 13 the period-radius relation for contact binaries (dashed lines) (Gazeas and Stępień 2008). The primary and secondary stars of QT UMa are indicated with an "X" in both figures. The primary star is more massive than predicted by the period-mass relation and slightly larger than predicted by the period-radius relation. Also included in Figures 12 and 13 are the masses and radii of three contact binaries (ER Ori, EF Boo, and AA UMa) that are very similar to QT UMa in terms of orbital period, primary and secondary masses, mass ratio,

Table 5. Comparison of QT UMa with similar W-type contact binaries.

Star	*Period (d)*	M_1	M_2	*q*	R_1	R_2	M_V	*References*
QT UMa	0.4735	0.872	1.490	1.707	1.172	1.320	3.86	—
ER Ori	0.4234	0.765	1.385	1.812	1.007	1.392	3.69	1, 2, 3
EF Boo	0.4295	0.792	1.547	1.953	1.026	1.424	3.46	1, 2, 3
AA UMa	0.4680	0.773	1.419	1.835	1.079	1.653	3.87	1, 2, 3

The masses and radii are in solar units ($M_\odot$ and $R_\odot$). References: 1. Gazeas and Stępień 2008; 2. Ammons et al. 2006; 3. Gaia Collaboration et al. 1, 2016.

radii, and absolute magnitudes. Listed in Table 5 are the well-determined geometrical and physical properties of these three stars. The absolute magnitudes in the table were calculated using Gaia parallaxes for distance with the observed visual apparent magnitudes corrected for extinction. The radius and mass of QT UMa are in good agreement with the properties of these three stars. The current evolutionary state of all four stars and their evolutionary histories may be very similar.

The O–C residuals in Figure 4 indicates the orbital period of QT UMa is increasing. The quadratic least-squares solution gives a period change rate of $dP/dt = 1.10(0.22) \times 10^{-6}$ d yr^{-1} (about 9.5 seconds per century), which is quite rapid compared to other binaries of this type. This result should be considered preliminary, given that the available times of minima only span five years. If this is a secular period change, then it likely results from conservative mass exchange from the lower mass primary star to the more massive secondary. In this case the rate of mass exchange would be $1.6\,(0.4) \times 10^{-6}\,M_\odot$ yr^{-1}. The observed period change could also result from light time effects as the binary orbits a third body. The O–C curve in Figure 4 may only be a portion of a sinusoidal ephemeris. Additional precision times of minima over several years would be invaluable in confirming the existence of the period change and in determining its cause. The study confirms QT UMa is a W-type eclipsing binary with the larger cooler secondary star eclipsing the smaller hotter star at primary minimum. As is typical for this class of stars, the primary star is over luminous compared to a single main-sequence star of the same mass. The WD solution gives a fill-out of 13%, which is consistent with a contact binary. The primary and secondary stars have spectral types of F9 and G8, respectively. The temperature difference of 556 K between the stars may indicate poor thermal contact. A future spectroscopic study of this system would provide the radial velocity measurements necessary for direct determination of the stellar masses.

6. Acknowledgements

This research was made possible through the use of the AAVSO Photometric All-Sky Survey (APASS), funded by the Robert Martin Ayers Sciences Fund. This research has made use of the SIMBAD database and the VizieR catalogue access tool, operated at CDS, Strasbourg, France.

References

Ammons, S. M., Robinson, S. E., Strader, J., Laughlin, G., Fischer, D., and Wolf, A. 2006, *Astrophys. J.*, **638**, 1004.

Astraatmadja, T. L., and Bailer-Jones, C. A. L. 2016, *Astrophys. J.*, **833**, 119.

Bradstreet, D. H., and Steelman, D. P. 2002, *Bull. Amer. Astron. Soc.*, **34**, 1224.

Diethelm, R. 2012, *Inf. Bull. Var. Stars*, No. 6029, 1.

Diethelm, R. 2013, *Inf. Bull. Var. Stars*, No. 6063, 1.

Gaia Collaboration, *et al.* 2016, *Astron. Astrophys.*, **595**, A2.

Gazeas, K., and Stępień, K. 2008, *Mon. Not. Roy. Astron. Soc.*, **390**, 1577.

Henden, A. A., *et al.* 2015, AAVSO Photometric All-Sky Survey, data release 9, (https//:www.aavso.org/apass).

Hoffman, D. I., Harrison, T. E., and McNamara, B. J. 2009, *Astron. J.*, **138**, 466.

Hübscher, J. 2013, *Inf. Bull. Var. Stars*, No. 6084, 1.

Hübscher, J. 2016, *Inf. Bull. Var. Stars*, No. 6157, 1.

Hübscher, J. 2017, *Inf. Bull. Var. Stars*, No. 6196, 1.

Hübscher, J., and Lehmann, P. B. 2015, *Inf. Bull. Var. Stars*, No. 6149, 1.

Jester, S. *et al.* 2005, *Astron. J.*, **130**, 873.

Juryšek, J. *et al.* 2017, *Open Eur. J. Var. Stars*, **179**, 135.

Kafka, S. 2016, variable star observations from the AAVSO International Database, (https://www.aavso.org/aavso-international-database).

Lucy, L. B. 1968, *Astrophys. J.*, **151**, 1123.

Lucy, L. B., and Wilson, R. E. 1979, *Astrophys. J.*, **231**, 502.

Luo, A-Li, *et al.* 2015, *Res. Astron. Astrophys.*, **15**, i.d. 1095.

Mirametrics. 2015, Image Processing, Visualization, Data Analysis, (http://www.mirametrics.com).

Mochnacki, S. W. 1981, *Astrophys. J.*, **245**, 650.

Nagai, K. 2016, *Bull. Var. Star Obs. League Japan*, No. 61, 7.

Nelson, R. H. 2013, *Inf. Bull. Var. Stars*, No. 6050, 1.

Otero, S. A., Wils, P., and Dubovsky, P. A. 2004, *Inf. Bull. Var. Stars*, No. 5570, 1.

Pecaut, M. J., and Mamajek, E. E. 2013, *Astrophys. J., Suppl. Ser.*, **208**, 9 (http://www.pas.rochester.edu/~emamajek/EEM_dwarf_UBVIJHK_colors_Teff.txt).

Ruciński, S. M. 1969, *Acta Astron.*, **19**, 245.

Samolyk, G. 2016a, *J. Amer. Assoc. Var. Star Obs.*, **44**, 69.

Samolyk, G. 2016b, *J. Amer. Assoc. Var. Star Obs.*, **44**, 164.

Schlafly, E. F., *et al.* 2014, *Astrophys. J.*, **789**, 15 (http://faun.rc.fas.harvard.edu/eschlafly/2dmap/querymap.php).

Sichervskij, S. G. 2017, *Astrophys. Bull.*, **72**, 51.

van Hamme, W. 1993, *Astron. J.*, **106**, 2096.

van Hamme, W., and Wilson, R. E. 1998, *Bull. Amer. Astron. Soc.*, **30**, 1402.

Wilson, R. E., and Biermann, P. 1976, *Astron. Astrophys.*, **48**, 349.

Wilson, R. E., and Devinney, E. J. 1971, *Astrophys. J.*, **166**, 605.

Wozniak, P. R., *et al.* 2004, *Astron. J.*, **127**, 2436.